# Imaging Ferroelectrics

Maguire, Jesi R.; Waseem, Hamza; Mcquaid, Raymond G. P.; Kumar, Amit; Gregg, J. Marty; Cochard, Charlotte

*DOI:*
10.1002/aelm.202101384

*Publication date:*
2022

ADVANCED ELECTRONIC MATERIALS
www.advelectronicmat.de

# Imaging Ferroelectrics: Reinterpreting Charge Gradient Microscopy as Potential Gradient Microscopy

*Jesi R. Maguire, Hamza Waseem, Raymond G. P. McQuaid, Amit Kumar, J. Marty Gregg,* and Charlotte Cochard**

**Charge gradient microscopy (CGM) is a scanning probe imaging mode, particularly well-suited for the characterization of ferroelectrics. The implementation of the technique is straightforward; it involves monitoring currents that spontaneously develop between a passive conducting atomic force microscopy tip and Earth, as the tip is scanned across the specimen surface. However, details on the fundamental origin of contrast and what images mean, in terms of associated ferroelectric microstructures, are not yet fully understood. Here, by comparing information from CGM and Kelvin probe force microscopy, obtained from the same sets of ferroelectric domains (in both lithium niobate and barium titanate), it is shown that CGM reasonably reflects the spatial derivative of the measured surface potential. This is conceptually different from measuring local gradients in the surface bound-charge density or in any associated screening charges: after all, clear CGM signals are seen, even when polarization is entirely in-plane (where the bound charge density is uniformly zero, but gradients in surface potential are still fully expected). It is therefore suggested that CGM in ferroelectrics may be more accurately called potential gradient microscopy.**

## 1. Introduction

Historically, technological developments in microscopy have been extremely important for underpinning new insights into the nature and behavior of ferroelectric materials. Over the last few decades, this has perhaps been most strikingly illustrated by the way in which aberration-corrected transmission electron microscopy (TEM) has facilitated picometer resolution images of local dipole vectors. Flux-closure,[1] vortex,[2] and even skyrmion structures[3] have been stunningly revealed. In addition, the combination of TEM with focused ion beam microscope machining has allowed the response of ferroelectric domain patterns to complex nanoscale morphology to be firmly established.[4,5] The crucial importance of advances in scanning probe microscopy (SPM) should also be fully recognized: piezoresponse force microscopy (PFM) and its precursors have revolutionized the way in which ferroelectric domain microstructures can be mapped[6–9] and their dynamics studied;[10–14] conducting atomic force microscopy (cAFM) has been the breakthrough tool for unequivocally showing that domain walls can have very different transport characteristics from the domains that they surround,[15–20] and scanning nitrogen-vacancy magnetometry has exquisitely revealed spin cycloid microstructures in multiferroics[21] and has even been suggested as a future technique for examining local transient magnetic fields, expected during ferroelectric domain wall motion.[22]

One of the most recently discovered SPM imaging modes, relevant for ferroelectric characterization (first reported by Hong et al.[23] in 2014), is charge gradient microscopy (CGM). Practically, CGM involves scanning a cAFM tip (usually solid platinum), in contact mode at a relatively high set-point, so that a firm connection between tip and sample is maintained. Imaging is passive, in the sense that no deliberate external electrical signal is supplied. Instead, any currents that spontaneously develop and flow between the tip and Earth are simply measured and recorded as a function of tip position. A key observation is that, while the magnitude of local current may be increased by increasing the scan speed during imaging, the total integrated charge (flowing to or from Earth) is independent of the rate of tip motion relative to the sample surface. Contrast is therefore associated with the way in which the local tip-sample electrostatic interactions lead to changes in the charge state at the tip; such changes can be developed quickly (generating larger currents) or slowly (generating smaller currents), depending on the scanning rate used. As noted in

J. R. Maguire, H. Waseem, R. G. P. McQuaid, A. Kumar, J. M. Gregg
School of Mathematics and Physics
Queen's University Belfast
Belfast BT7 1NN, UK
E-mail: m.gregg@qub.ac.uk
C. Cochard
School of Science and Engineering
University of Dundee, Nethergate
Dundee DD1 4HN, UK
E-mail: CCochard001@dundee.ac.uk

The ORCID identification number(s) for the author(s) of this article can be found under https://doi.org/10.1002/aelm.202101384.



**DOI: 10.1002/aelm.202101384**

Hong et al.'s original paper, CGM gives strong signals from c+/c− 180° domain walls on z-cut periodically poled lithium niobate surfaces, where obvious spatial gradients in bound charge densities (and in any associated screening charge densities) should be expected.[23,24] Hence the name given to the imaging mode. The exact nature of the interactions between the tip and the ferroelectric surface that give rise to changes in the tip charge state, relative to Earth, is still a matter of some debate and the role of charged surface adsorbates seems to be particularly unclear.[23,25]

In this paper, we do not make comment on the detail of the interaction between the tip and the screening charge. Instead, we show that the integration of the CGM current, as a function of tip position, maps well to the experimentally determined spatial variation in the electrostatic potential, measured directly using Kelvin probe force microscopy (KPFM), for a number of different domain configurations: c+/c− 180° domains in periodically poled z-cut lithium niobate (with polarization vectors perpendicular to the imaged surface), head-to-head 180° domains in x-cut lithium niobate (with polarization vectors approximately parallel to the imaged surface) and a–c domains in {100} polished barium titanate (with polarization alternately oriented parallel and perpendicular to the imaged surface). We also consider the important implications of CGM signals found in mapping $a_1$–$a_2$ domains in $BaTiO_3$. Results suggest that, while the CGM technique undoubtedly monitors changes in the charge state of the conducting tip, this charge state is more directly related to spatial variations in the surface potential of the ferroelectric than to spatial variations in the surface bound charge density (or the density of any associated screening charges) under the tip. In this sense, CGM should be viewed as effectively imaging potential gradients, rather than charge gradients, on the ferroelectric surface.

## 2. Results and Discussion

Initially, we established CGM images, similar to those obtained by Hong et al.,[23] on z-cut periodically poled lithium niobate single crystals. Confirming their original observations,[23] the correlation between the spatial occurrence of currents and the domain walls separating 180° domains (measured by PFM) was found to be obvious (**Figure 1**a,c,e). However, CGM contrast on engineered head-to-head domain walls in x-cut lithium niobate, where the polarization is almost entirely parallel to the imaged surface, was seen to be dramatically different (Figure 1b,d,f). Instead of current peaks at the domain walls, where the spatial orientation of polarization changes, here the dominant response was that the current was almost constant within each domain but changed sign as the polarization orientation reversed (seen clearly in the color contrast in Figure 1d). In detail, a peak at the wall was also present (Figure 1f); however, we attribute this to a slight miscut angle, introduced by our inexact surface polishing, creating a small component of polarization out of the plane, which reverses sense across the domain wall.

These observations on lithium niobate (both z and x-cut) mirror those seen previously by Guy et al.,[26] where the link between CGM current and the change, or gradient, in surface potential (rather than the change in uncompensated bound charge at the surface) was first suspected. In Guy et al., local potential variations were, however, solely informed by finite element modeling. Here, we generate more meaningful insight by comparing CGM information with experimentally determined surface potentials, measured directly using KPFM. We thereby show our initial ideas to be experimentally verified.

KPFM imaging of ferroelectric surfaces in ambient conditions is a challenge, as surface adsorbates, which screen the local potential, accumulate over a timescale of between seconds and minutes. The KPFM images shown in **Figure 2**c,d were obtained directly after the domains had been imaged in contact mode (panels (a) and (b)) to clean the surface, by physically scraping most of such adsorbates away. Correlations between the potential contrast and the domain contrast are obvious. More subtle insight is, however, revealed by turning the slow-scan axis off and accumulating signal from repeated scans along the same line-trace, to increase the signal-to-noise ratio in the data. In **Figure 3**, KPFM line scans, taken perpendicular to the surface-trace of domain walls, for both c+/c− domains in z-cut lithium niobate (Figure 3a) and in-plane head-to-head domains in x-cut lithium niobate (Figure 3b), are presented. Rather than comparing these data to the raw CGM traces, they are instead compared to the spatial integrals of the CGM currents (Figure 3c,d). For c+/c− domains, both the KPFM surface potential and the integrated CGM currents show peaks above domains with downward orientations of polarization and troughs above those with upward oriented polarization (Figure 3a,c). Equally, for the head-to-head in-plane domains, KPFM reveals a strong "V"-shaped function, with the potential being at a minimum close to the wall (Figure 3b). The same kind of "V" is seen for the spatial integration of the CGM currents, taken from the same microstructural region (Figure 3d). While the match is not perfect, the strong similarity in the form of these functions is clearly evident. We are therefore left with the following observation

$$V \equiv \int_{x_1}^{x_2} \frac{dV}{dx}\,\mathrm{d}x = k\int_{x_1}^{x_2} I_{CGM}\,\mathrm{d}x \tag{1}$$

where $x$ is the position along the line-scan, $V$ is the local surface potential measured by KPFM in a small region (pixel) bounded by points $x_1$ and $x_2$, and $I_{CGM}$ is the locally measured CGM current; $k$ is a proportionality constant dependent on the microscope setup. The implication from Equation (1) is that the CGM current is proportional to the gradient in the surface potential along the scanning direction

$$I_{CGM} \propto \frac{dV}{dx} \tag{2}$$

To test this notion further, CGM and KPFM information was obtained for another set of domains, with both in-plane and out-of-plane polarization present: a–c stripe domains in $\{100\}_{\text{pseudocubic}}$ polished single-crystal $BaTiO_3$. The typical surface domain microstructure can be seen in the PFM map presented in **Figure 4**a. While the CGM maps (Figure 4b) show stripe-like features which clearly correlate with the PFM microstructure, there is unexpected complexity apparent in the contrast. When the

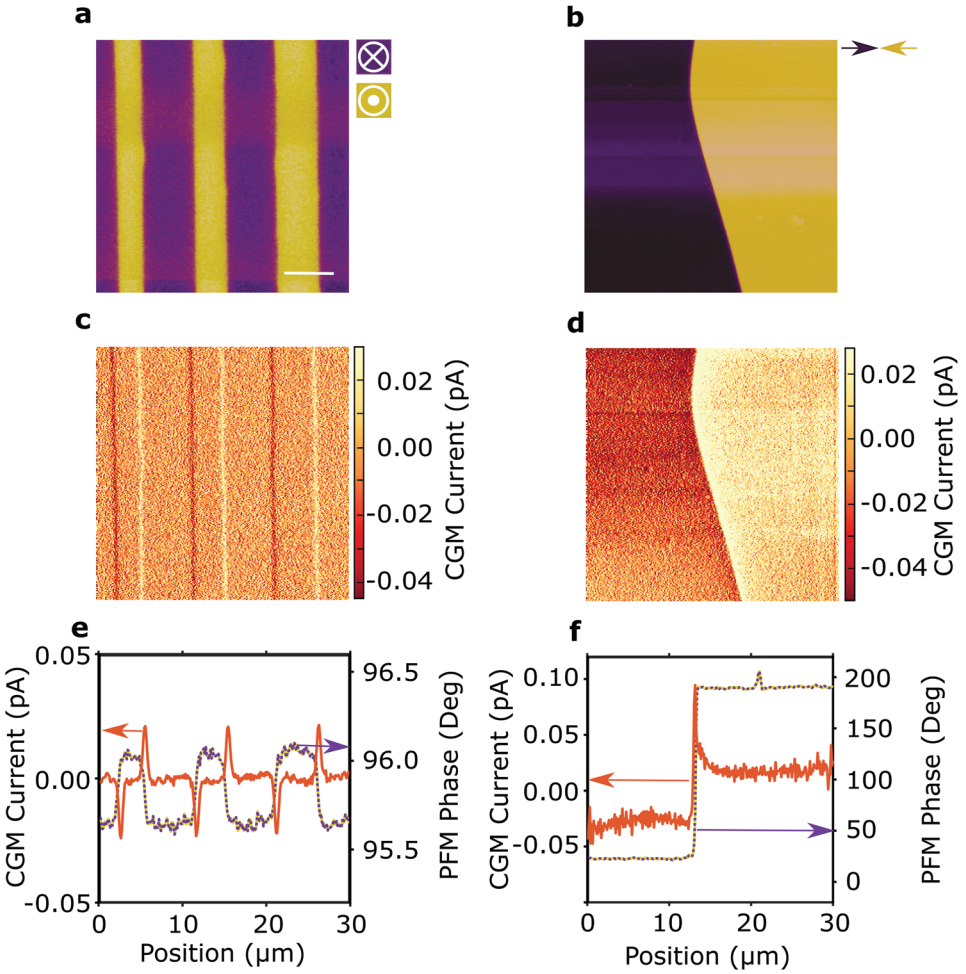


**Figure 1.** CGM of domains in lithium niobate (LNO). Piezoresponse force microscopy (PFM) phase maps of a) c+/c– domains, with polarization approximately perpendicular to the surface, in z-cut periodically poled LNO (vertical PFM) and b) head-to-head charged domain wall region, with polarization approximately parallel to the surface, in x-cut LNO (lateral PFM). Corresponding CGM map for c) c+/c– domains and d) head-to-head charged domain wall region. All images are shown at the same magnification and the scale bar in (a) is 6 μm long. e,f) Line trace information, taken approximately perpendicular to the surface traces of the domain walls, showing CGM data (orange), summed over multiple scan lines with the slow scan axis disabled, along with PFM phase variations (to help identify the positions of domain walls).

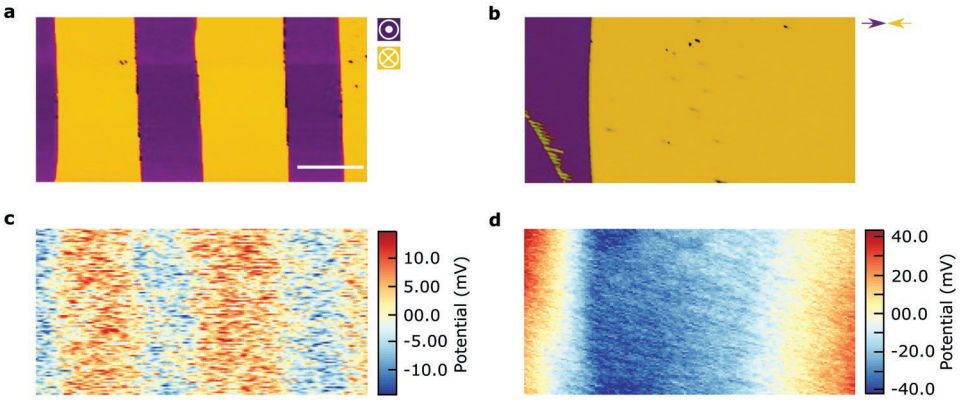


**Figure 2.** KPFM of lithium niobate domains. PFM phase maps for a) c+/c– domains, with polarization approximately perpendicular to the surface, in z-cut periodically poled LNO (vertical PFM) and b) head-to-head charged domain wall region, with polarization approximately parallel to the surface, in x-cut LNO (lateral PFM), along with c,d) associated surface potential maps, measured using KPFM. Images are all at the same magnification and the scale bar (in (a)) is 4.7 μm long.

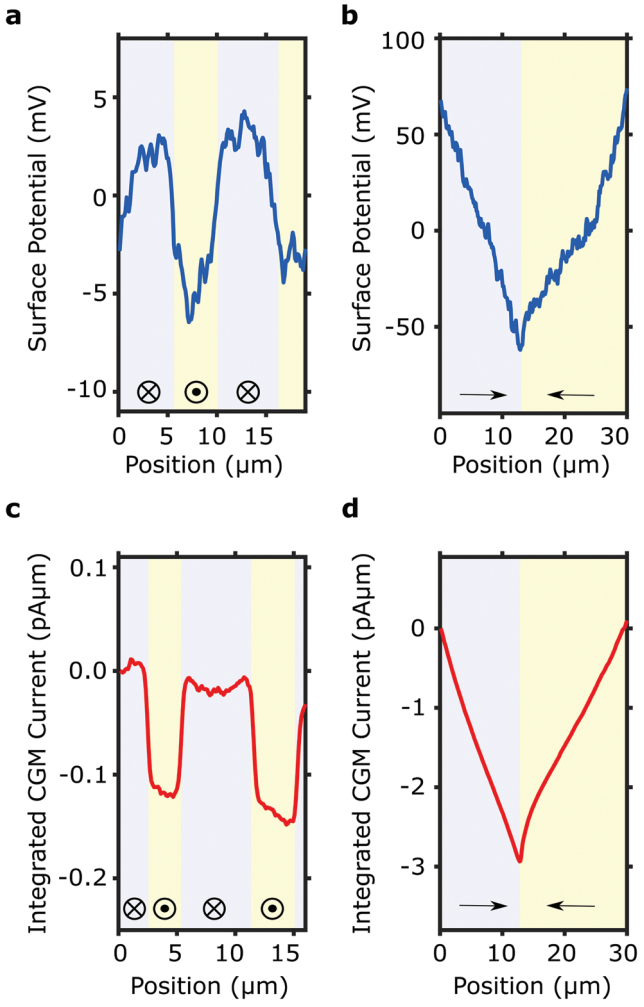


**Figure 3.** Line traces comparing the measured surface potential with the spatial integration of the CGM current. KPFM surface potential variations associated with a) c+/c– domains in z-cut periodically poled LNO and b) the head-to-head charged domain wall region in x-cut LNO, along with corresponding plots c,d) generated by integrating the CGM currents with respect to distance along the scan direction. Similarities between the measured potential and the integrated CGM current are obvious. Background colors represent different domain orientations with local polarization directions as indicated by arrows.

CGM current response is averaged over a number of a–c periods and then spatially integrated, an "idealized" version of what the surface potential might look like can be created, assuming that Equation (1) and its implications are true (Figure 4c).

The directly measured potential (obtained with KPFM) is shown in Figure 4d. Despite the complexity in the functions, the similarity between the spatially integrated CGM current and the measured surface potential is striking. Both show a monotonic increase across the width of the a-domain, with a change of gradient close to its midpoint and both show a nonmonotonic decrease in potential across the width of the c-domain with a local minimum and an off-centered rounded maximum. Again, the CGM current is observed to correspond closely to the gradient in the measured surface potential.

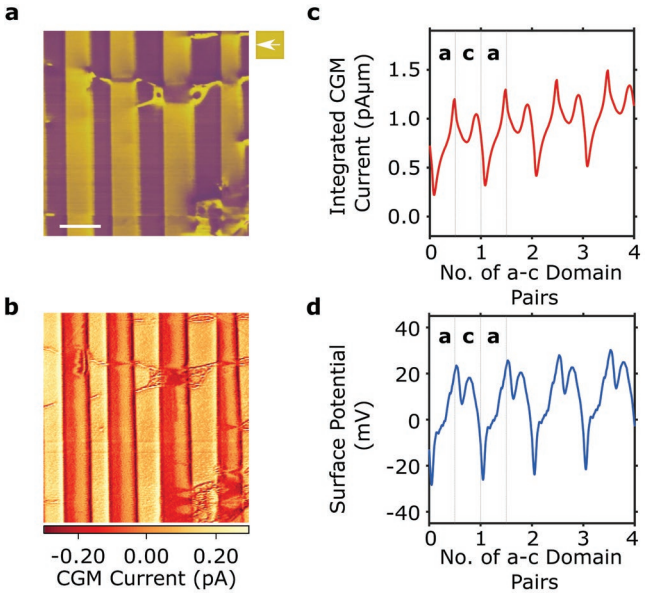


**Figure 4.** Relationship between the CGM current and surface potential for a more complex set of domain variants (a/c domains in barium titanate). a) Lateral PFM phase image (arrow indicates in-plane polarization orientation of the a-domains which are rendered in yellow) and b) CGM current map from the same area. The scale bar in (a) is 4.8 μm long and applies equally to panel (b). The slow-scan axis was turned off and CGM data were collected over multiple line scans. c) Averaged currents across a and c domains were calculated and then stitched together to produce an idealized version of the integrated CGM current for a number of a–c domain pairs. d) The measured surface potential variations (using KPFM) across a and c domains were also averaged and then stitched together in a similar manner. The similarity between the integrated CGM current and the measured KPFM potential is again evident.

In cases where there is an out-of-plane component in the polarization, gradients in bound charge and gradients in surface potential can be conflated. In order to further demonstrate that CGM currents are most likely to arise because of gradients in the surface potential, let us consider results from $a_1$–$a_2$ ferroelastic domains in $BaTiO_3$. Here, the ferroelectric polarization is entirely in-plane. The bound charge density ($\sigma_b$) on the surface is equal to zero ($\sigma_b = P \cdot \hat{n} = 0$, where $P$ is the polarization vector and $\hat{n}$ is the unit vector perpendicular to the surface). Hence, there is neither bound charge density at, nor bound charge density gradients across, the free surface. By contrast, there is a potential gradient ($\nabla V$), which is parallel to $P$ ($|P| \propto |\nabla V|$), and associated equipotential lines on the surface, that are perpendicular to $P$.

The situation is summarized by the plan-view schematic, in **Figure 5**a, of an $a_1$–$a_2$ surface region, mapped by CGM. When horizontal CGM line scans (left-to-right traces in the schematic) are performed, the scanning vector is antiparallel to $P$ (hence is perpendicular to equipotential lines), in one of the domain types, and perpendicular to $P$ (along equipotential lines) in the other domain type. In the former case, a linearly changing potential (constant potential gradient) is experienced by the moving tip and this produces an approximately constant CGM current (Figure 5b,c). In the latter, no gradient in potential is sampled and no CGM currents beyond the noise floor arise. Given the absence of bound charge density and the fact that

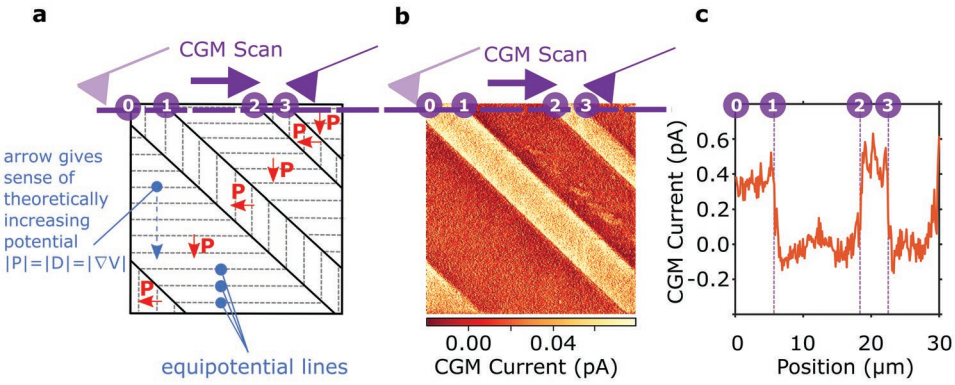


**Figure 5.** CGM current mapping of $a_1$–$a_2$ domains on a {100} $BaTiO_3$ surface. a) Plan view schematic of one of the surface regions mapped by CGM in {100} $BaTiO_3$ containing ferroelastic $a_1$-$a_2$ domains, with polarizations entirely in-plane. Note the entire surface has a bound charge density of zero, as the polarization is perpendicular to the surface-normal. However, the potential at the surface is expected to vary. To help visualize the potential variation, equipotential lines have been marked (gray dashed lines) which are perpendicular to the polarization vector. CGM scans (map in (b) and individual line-scan in (c)) show clear variations in the current: constant magnitude for domains in which the sensing tip cuts equipotential lines and zero in domains where the scanning tip runs parallel to the equipotential lines. These data show that the CGM signal relates to the potential gradient measured at the surface and not the bound charge density gradient (as none exists in this instance).

CGM currents arise only when equipotential lines are crossed, we must conclude that it is the potential gradients that are responsible for the CGM signal.

An aspect of the experimental work that should also be discussed concerns the signs of the CGM current, inferred surface potential determined by spatial integration of the CGM, and the directly measured surface potential. In **Figure 6**, we have used finite element simulation (Comsol Multiphysics) to calculate the surface potential of lithium niobate for both c+/c– domains in the z-cut crystal and for the approximately in-plane head-to-head domain wall region in the x-cut crystal, in the absence of any screening (equivalent to vacuum). In the former case, domains with polarization pointing out-of-the-plane have positive surface potentials, while those pointing into the plane have negative surface potentials. This is exactly opposite to the KPFM potential map shown in Figure 2c (and line scan in Figure 3a) and to the integrated CGM profile shown in Figure 3c. Correspondingly, the calculated potential gradient (Figure 6b,c) is negative moving from an "up" polarized state to a "down" one, whereas the corresponding measured CGM current (Figure 1e) is positive. For the head-to-head domain wall region in the x-cut lithium niobate, the calculated potential (Figure 6d,f) is a triangular function that is maximized at the wall, whereas in integrated CGM and in directly measured KPFM measurements (Figure 3b,d), the triangular function is inverted (with a minimum at the wall). The associated CGM currents are also opposite in sign to those of the calculated potential gradients (compare Figure 1d,f to Figure 6e,f). In short, while the CGM and KPFM information is internally self-consistent, all inferred surface potentials are opposite in sign to those expected from modeling.

We have tested the KPFM in our scanning probe microscope, by monitoring the potential above a thin film electrode connected to a voltage source, and it was found to be entirely accurate. We must therefore conclude that the measured surface potential (spatially integrated CGM and KPFM) is genuinely opposite in sign to that expected in the absence of screening. It should be noted that this is commonly observed in the published literature[27–34] and in ambient imaging should, perhaps, be fully expected.

## 3. Conclusion

By using scanning probe microscopy to examine different ferroelectric domain patterns, we present evidence that currents measured by CGM are generated by gradients in electrostatic surface potential, rather than gradients in surface bound charge densities. This is best illustrated when the spatial integration of the CGM current is compared to the surface potential measured directly by KPFM. The insight makes the interpretation of CGM information relatively straightforward, as it simply offers an alternative to KPFM for determining the surface potential in some materials and in some circumstances. A possible advantage of the technique is that the strong tip-sample contact needed for CGM measurements means that surface potentials can be accessed even in environments where rapid accumulation of screening adsorbates would normally occur, which could obscure KPFM contrast completely—the CGM scanning continually scrapes most of these adsorbates away. However, there are distinct disadvantages too: CGM could not, e.g., be used to monitor potential gradients in a charged metallic sheet, as the tip contact would produce a short to Earth; this would facilitate discharge, and hence completely change the potential as a result.

## 4. Experimental Section

*Charge Gradient Microscopy*: CGM experiments were performed using an Asylum MFP-3D Infinity AFM system in the current-sensing mode (ORCA). The technique involved rastering a grounded conductive probe (25Pt300B from Rocky Mountain Nanotechnology) across the surface of a grounded sample at high scan speeds (≈0.5 mm $s^{-1}$) with a high deflection setpoint or tip pressure (18 V, ≈2 μN force), while passively measuring any current that flows. The sign of the current flow depended on the scanning direction of the probe and reflected local

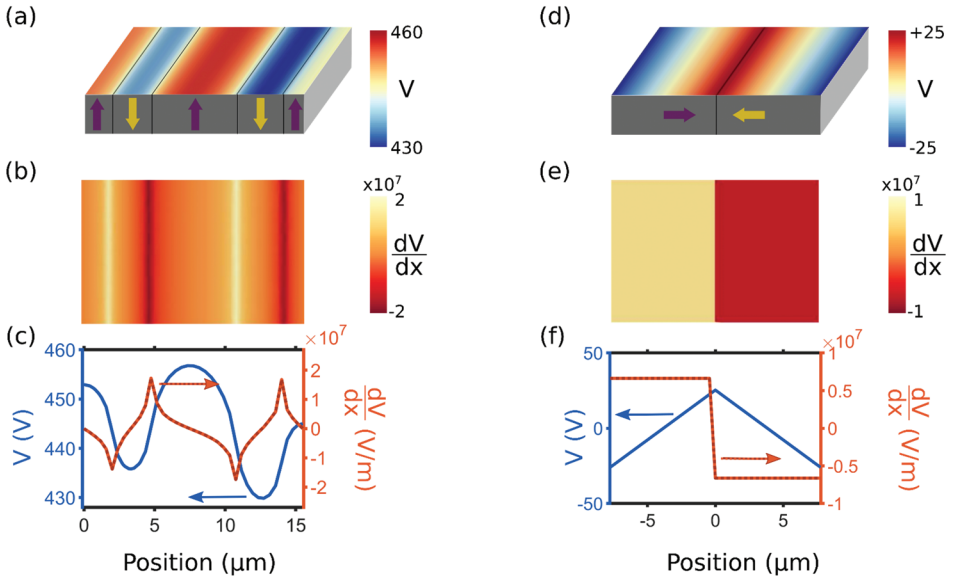


**Figure 6.** Finite element simulation of the surface potential and associated gradients for LNO. a,d) Color maps of the surface potential *V*, b,e) color maps of the positional derivative of the surface potential $\frac{dV}{dx}$, and c,f) comparison of the line profiles along *x* of the surface potential *V* (blue) and spatial derivative $\frac{dV}{dx}$ (dotted orange). The spatial derivatives of the potential scale with the measured CGM but are inverted in sign.

changes in the electrostatic potential on the surface of the sample. Offset currents induced by the experimental set-up were removed.

*Kelvin Probe Force Microscopy*: KPFM experiments were performed using the same AFM system. In these studies, a Pt/Ir-coated Si probe, with a resonance frequency of ≈70 kHz (Nanosensors, PPP-EFM), was used. KPFM is a two-pass technique, in which the surface topography is mapped during the first pass via conventional tapping mode, before withdrawing to a fixed height above the surface (20 nm for these experiments) for the second pass. During this second pass, a dc bias was applied to the probe such that it matched the contact potential difference between the probe and sample surface. This was done by nullifying the vibration of the probe, which was initially driven by the electrostatic force induced on the AFM probe, giving a true measurement of the local surface potential.

*Piezoresponse Force Microscopy*: PFM experiments were performed with solid Pt probes (25Pt300B from Rocky Mountain Nanotechnology) using the MFP's internal lock-in amplifier. Imaging was carried out near resonance, with a frequency of ≈100 kHz for observing out-of-plane domains and ≈200 kHz for in-plane domains. AC biases between 1 and 5 V were used for these measurements.

Validation of the domain structure was carried out using a Veeco Dimension 3100 AFM system (equipped with Nanoscope IIIa controller) in conjunction with an EG&G 7265 lock-in amplifier. For these experiments, Pt/Ir-coated Si probes (Nanosensors, PPP-EFM) were used and measurements were undertaken away from resonance at 20 kHz with applied AC biases between 1 and 5 V. Rotating the crystal orientation allowed for the relative polarization orientations to be unequivocally determined using vector PFM (combination of vertical and lateral PFM).

*Modeling of Electrostatic Potential from Finite Element Modeling*: Comsol Multiphysics 5.4 was used to model the static electrostatic potential at the surface of dielectric materials with a spontaneous polarization. The exterior boundary conditions were consistent with what would happen in vacuum, while the interior boundaries were set for the continuity of the dielectric displacements. The mesh used consisted of tetrahedra with the largest dimension smaller than 1 μm and routinely one to two orders of magnitude lower. Simulations were stopped when convergence lower than 0.001 was obtained. The geometry was set to reproduce fairly the experimental geometry: a parallelepiped with width 10 μm, thickness 500 μm, and length between 20 and 40 μm depending on the domain patterns. The thickness was chosen to be similar to the experimental thickness; the depth was irrelevant because of the symmetry of the experiment and the width of each domain was chosen to match experiments.

## Acknowledgements

The authors acknowledge funding to support the research from the Engineering and Physical Sciences Research Council (EPSRC) in the UK (EP/P02453X/1) and from the Department for Employment (DfE) in Northern Ireland. RGPMcQ acknowledges support from a UKRI Future Leaders Fellowship (MR/T043172/1). The authors also thank Elizabeth Soergel (University of Bonn) for providing one of the $LiNbO_3$ crystals used in the study.

## Conflict of Interest

The authors declare no conflict of interest.

## Data Availability Statement

The data that support the findings of this study are available from the corresponding author upon reasonable request and will also be made openly available in University of Dundee Discovery at https://doi.org/10.15132/10000175.

## Keywords

charge gradient microscopy, domains, ferroelectrics

Received: December 22, 2021
Revised: February 18, 2022
Published online:

[1] Y. L. Tang, Y. L. Zhu, X. L. Ma, A. Y. Borisevich, A. N. Morozovska, E. A. Eliseev, W. Y. Wang, Y. J. Wang, Y. B. Xu, Z. D. Zhang, S. J. Pennycook, *Science* **2015**, *348*, 547.
[2] A. K. Yadav, C. T. Nelson, S. L. Hsu, Z. Hong, J. D. Clarkson, C. M. Schlepütz, A. R. Damodaran, P. Shafer, E. Arenholz, L. R. Dedon, D. Chen, A. Vishwanath, A. M. Minor, L. Q. Chen, J. F. Scott, L. W. Martin, R. Ramesh, *Nature* **2016**, *530*, 198 .
[3] S. Das, Y. L. Tang, Z. Hong, M. A. P. Gonçalves, M. R. McCarter, C. Klewe, K. X. Nguyen, F. Gómez-Ortiz, P. Shafer, E. Arenholz, V. A. Stoica, S.-L. Hsu, B. Wang, C. Ophus, J. F. Liu, C. T. Nelson, S. Saremi, B. Prasad, A. B. Mei, D. G. Schlom, J. Íñiguez, P. García-Fernández, D. A. Muller, L. Q. Chen, J. Junquera, L. W. Martin, R. Ramesh, *Nature* **2019**, *568*, 368.
[4] A. Schilling, D. Byrne, G. Catalan, K. G. Webber, Y. A. Genenko, G. S. Wu, J. F. Scott, J. M. Gregg, *Nano Lett.* **2009**, *9*, 3359 .
[5] A. Schilling, R. M. Bowman, G. Catalan, J. F. Scott, J. M. Gregg, *Nano Lett.* **2007**, *7*, 3787.
[6] P. Güthner, K. Dransfeld, *Appl. Phys. Lett.* **1992**, *61*, 1137.
[7] M. Abplanalp, L. M. Eng, P. Gunter, *Appl. Phys. A: Mater. Sci. Process.* **1998**, *66*, S231.
[8] S. V. Kalinin, D. A. Bonnell, *Phys. Rev. B* **2002**, *65*, 125408.
[9] *Ferroelectrics at Nanoscale: Scanning Probe Microscopy Approach* (Eds: M. Alexe, A. Gruverman), Springer, New York **2004**.
[10] A. Gruverman, D. Wu, J. F. Scott, *Phys. Rev. Lett.* **2008**, *100*, 097601.
[11] Y. Kim, H. Han, W. Lee, S. Baik, D. Hesse, M. Alexe, *Nano Lett.* **2010**, *10*, 1266.
[12] P. Sharma, Raymond G. P., McQuaid, L. J., McGilly, J., M. Gregg, A. Gruverman, *Adv. Mater.* **2013**, *25*, 1323.
[13] J. R. Whyte, R. G. P. McQuaid, P. Sharma, C. Canalias, J. F. Scott, A. Gruverman, J. M. Gregg, *Adv. Mater.* **2014**, *26*, 293.
[14] J. R. Whyte, J. M. Gregg, *Nat. Commun.* **2015**, *6*, 7361.
[15] J. Seidel, L. W. Martin, Q. He, Q. Zhan, Y.-H. Chu, A. Rother, M. E. Hawkridge, P. Maksymovych, P. Yu, M. Gajek, N. Balke, S. V. Kalinin, S. Gemming, F. Wang, G. Catalan, J. F. Scott, N. A. Spaldin, J. Orenstein, R. Ramesh, *Nat. Mater.* **2009**, *8*, 229.
[16] J. Guyonnet, I. Gaponenko, S. Gariglio, P. Paruch, *Adv. Mater.* **2011**, *23*, 5377.
[17] M. Schröder, A. Haußmann, A. Thiessen, E. Soergel, T. Woike, L. M. Eng, *Adv. Funct. Mater.* **2012**, *22*, 3936.
[18] D. Meier, J. Seidel, A. Cano, K. Delaney, Y. Kumagai, M. Mostovoy, N. A. Spaldin, R. Ramesh, M. Fiebig, *Nat. Mater.* **2012**, *11*, 284.
[19] R. G. P. McQuaid, M. P. Campbell, R. W. Whatmore, A. Kumar, J. M. Gregg, *Nat. Commun.* **2017**, *8*, 15105.
[20] Y. S. Oh, X. Luo, F.-T. Huang, Y. Wang, S.-W. Cheong, *Nat. Mater.* **2015**, *14*, 407.
[21] I. Gross, W. Akhtar, V. Garcia, L. J. Martinez, S. Chouaieb, K. Garcia, C. Carrétéro, A. Barthélémy, P. Appel, P. Maletinsky, J.-V. Kim, J. Y. Chauleau, N. Jaouen, M. Viret, M. Bibes, S. Fusil, V. Jacques, *Nature* **2017**, *549*, 252.
[22] D. M. Juraschek, Q. N. Meier, M. Trassin, S. E. Trolier-McKinstry, C. L. Degen, N. A. Spaldin, *Phys. Rev. Lett.* **2019**, *123*, 127601.
[23] S. Hong, S. Tong, W. I. Park, Y. Hiranaga, Y. Cho, A. Roelofs, *Proc. Natl. Acad. Sci. U. S. A.* **2014**, *111*, 6566.
[24] J. M. Gregg, A. Kumar, *Nature* **2014**, *510*, 481.
[25] Y. Y. Choi, S. Tong, S. Ducharme, A. Roelofs, S. Hong, *Sci. Rep.* **2016**, *6*, 25087.
[26] J. G. M. Guy, C. Cochard, P. Aguado-Puente, E. Soergel, R. W. Whatmore, M. Conroy, K. Moore, E. Courtney, A. Harvey, U. Bangert, A. Kumar, R. G. P. McQuaid, J. M. Gregg, *Adv. Mater.* **2021**, *33*, 2008068.
[27] X. Q. Chen, H. Yamada, T. Horiuchi, K. Matsushige, S. Watanabe, M. Kawai, P. S. Weiss, *J. Vac. Sci. Technol., B: Microelectron. Nanometer Struct.–Process., Meas., Phenom.* **1999**, *17*, 1930.
[28] N. Domingo, I. Gaponenko, K. Cordero-Edwards, N. Stucki, V. Pérez-Dieste, C. Escudero, *Nanoscale* **2019**, *11*, 17920.
[29] Y. Kim, C. Bae, K. Ryu, H. Ko, Y. K. Kim, S. Hong, H. Shin, *Appl. Phys. Lett.* **2009**, *94*, 032907.
[30] S. V. Kalinin, C. Y. Johnson, D. A. Bonnell, *J. Appl. Phys.* **2002**, *91*, 3816.
[31] S. V. Kalinin, D. A. Bonnell, *Phys. Rev. B* **2001**, *63*, 125411.
[32] S. V. Kalinin, D. A. Bonnell, *Appl. Phys. Lett.* **2001**, *78*, 1116.
[33] S. V. Kalinin, D. A. Bonnell, *Nano Lett.* **2004**, *4*, 555 .
[34] S. V. Kalinin, D. A. Bonnell, *Phys. Rev. B* **2004**, *70*, 235304.